

pubs.acs.org/cm Article

Evolution of Yb³⁺ Speciation in Cl⁻/Br⁻- and Yb³⁺/Gd³⁺-Alloyed Quantum-Cutting Lead-Halide Perovskite Nanocrystals

Joo Yeon D. Roh, David E. Sommer, Tyler J. Milstein, Scott T. Dunham, and Daniel R. Gamelin*



Cite This: Chem. Mater. 2023, 35, 8057-8064



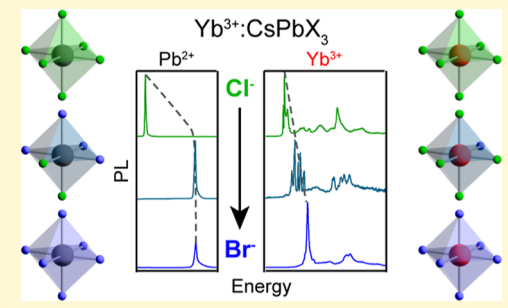
ACCESS

III Metrics & More

Article Recommendations

SI Supporting Information

ABSTRACT: Ytterbium-doped all-inorganic lead-halide perovskites $(Yb^{3+}:CsPb-(Cl_{1-x}Br_x)_3)$ generate near-infrared photoluminescence (PL) quantum yields exceeding 100% by quantum cutting. Experimental and computational studies have suggested complex dopant speciation in these materials arising from the formation of lattice defects needed to compensate for the excess charge of Yb^{3+} relative to Pb^{2+} , but the relationship between quantum cutting and such speciation is still poorly understood. Here, we use cryogenic photoluminescence spectroscopy and density functional theory-assisted kinetic Monte Carlo simulations to investigate changes in Yb^{3+} speciation induced by anion $(Cl^-$ vs $Br^-)$ and trivalent-dopant $(Yb^{3+}$ vs $Gd^{3+})$ alloying in $CsPb(Cl_{1-x}Br_x)_3$ $(0.00 \le x \le 1.00)$ perovskite nanocrystals (NCs). The experimental results reveal nonstatistical distributions of



Yb-Cl and Yb-Br bonds in Yb³⁺:CsPb(Cl_{1-x}Br_x)₃ NCs. Monte Carlo simulations reproduce the experimental trends well and predict thermodynamic favorability for Yb³⁺ dopants to retain Cl⁻ coordination, even in the presence of high lattice Br⁻ concentrations. For a given lattice composition (e.g., CsPbCl₃), low-temperature PL spectra reveal that the relative populations of three dominant Yb³⁺ species change substantially with Gd³⁺ codoping. These results further show that quantum cutting is largely insensitive to these differences in Yb³⁺ speciation, ruling out any "magic" configuration of Yb³⁺ ions and defects. These results are discussed in relation to the microscopic prerequisites for the concerted sensitization of two Yb³⁺ ions during quantum cutting. Overall, these findings highlight the mechanistic robustness of Yb³⁺:CsPb(Cl_{1-x}Br_x)₃ quantum cutting in lead-halide perovskites and provide deeper insight into the inner workings of this unique phenomenon.

1. INTRODUCTION

Ytterbium-doped all-inorganic lead-halide perovskite $(Yb^{3+}:CsPb(Cl_{1-x}Br_x)_3)$ nanocrystals (NCs) have attracted broad research interest since the recent discovery of their remarkably high photoluminescence quantum yields (PLQYs), which can exceed 100% via quantum cutting. 1-8 This photomultiplication process converts the energy from an absorbed blue or ultraviolet (UV) photon to excite two Yb³⁺ dopant ions, which then re-emit that energy in the nearinfrared (NIR) at a wavelength that matches the bandgap of silicon solar cells. Yb³⁺:CsPb(Cl_{1-x}Br_x)₃ is unique among known quantum-cutting materials⁹⁻¹³ in that it combines the strong broadband absorption of a direct-gap semiconductor with the efficient luminescence of a lanthanide dopant, making it particularly attractive for solar harvesting and spectral conversion. Anion alloying within Yb^{3+} : $CsPb(Cl_{1-x}Br_x)_3$ (0.00 $\leq x \leq 1.00$) tunes the bandgap energy ($E_{\rm g}$) and hence the portion of the solar spectrum absorbed by the perovskite, but efficiency drops rapidly when $E_{\rm g}$ is reduced below the thermodynamic threshold for energy-conserving quantum cutting $(2 \times E_{f-f})$ at $x \approx 0.66$). These materials have already demonstrated substantial increases in the power conversion efficiencies of silicon and CIGS solar cells^{2,14} and offer the opportunity to improve upon the Shockley-Queisser thermodynamic limit of single-junction photovoltaics. 15

To advance such applications, fundamental studies of these materials in the forms of colloidal NCs, $^{1-3,5,6,8,14,19-23}$ single crystals (SCs), 23 and solution-processed and vapor-deposited thin films 4,24,25 remain essential.

Substitutional Yb³+ dopants require charge compensation, and experiment and computation both indicate that lead vacancies (V_{Pb}) constitute the primary defect allowing charge neutrality. Copputational work shows similar thermodynamics for various dopant-bound or dissociated defect configurations in Yb³+:CsPbCl₃. At high Yb³+ doping, where PLQYs are greatest, charge-neutral defect clusters (YbPb-VPb-YbPb, both linear and bent) are predicted to be the most prevalent. The identities and influence of these different species are still poorly understood. Multiple Yb³+ species are evident from low-temperature high-resolution PL spectra of Yb³+:CsPbCl₃ SCs and NCs, although one primary

Received: June 15, 2023 Revised: August 18, 2023 Published: September 20, 2023





Yb³⁺ species appears disproportionately active in quantum cutting.²³

Here, we report results from two sets of experiments aimed at using compositional changes to reveal aspects of Yb3+ speciation and its influence on PL sensitization in Yb3+:CsPb- $(Cl_{1-x}Br_x)_3$ NCs. Specifically, high-resolution low-temperature PL spectra of Yb³⁺:CsPb(Cl_{1-x}Br_x)₃ NCs have been measured as a function of anion alloying (0.00 $\leq x \leq$ 1.00) and B-site cation alloying (replacing Yb3+ with Gd3+) to observe the evolution of Yb3+ local environments in each compositional dimension. From the anion alloying experiments, the data reveal that Cl-to-Br anion exchange at Yb3+ lags behind that of the surrounding lattice, such that $[YbCl_6]^{3-}$ units remain prevalent even at $x \sim 0.50$. Computations reproduce the experimental trend well and show that this nonstatistical local coordination of Yb³⁺ is thermodynamically favorable. From the B-site alloying experiments, the data show that the introduction of Gd^{3+} codopants changes the relative probabilities of different Yb3+ species but that quantum cutting is largely undisturbed by this change, even though the population of correlated Yb3+ dopant pairs is (statistically) diminished. These results shed light on the microscopic environments around Yb3+ dopants involved in quantum cutting in Yb³⁺:CsPb(Cl_{1-x}Br_x)₃ NCs, and they demonstrate a substantially richer diversity of active Yb³⁺ sites than previously recognized.

2. EXPERIMENTAL SECTION

- **2.1. Materials.** Oleylamine (OAm, 70%, Sigma-Aldrich), oleic acid (OA, 90%, Sigma-Aldrich), 1-octadecene (ODE, 90%, Sigma-Aldrich), lead acetate trihydrate (Pb(OAc)₂·3H₂O, 99.999%, Sigma-Aldrich), gadolinium(III) acetate hydrate (99.9%, Gd(OAc)₃·xH₂O, Sigma-Aldrich), cesium acetate (CsOAc, 99.9%, Sigma-Aldrich), trimethylsilyl chloride (TMS-Cl, 98%, Acros Organics), trimethylsilyl bromide (TMS-Br, 97%, Sigma-Aldrich), anhydrous ethanol (EtOH, 200 proof, Decon Laboratories, Inc.), *n*-hexane (99%, Sigma-Aldrich), ethyl acetate (EtOAc, 99%, Sigma-Aldrich), and hydrochloric acid (HCl, Macron Fine Chemicals) were used as received unless otherwise noted. As-received ytterbium acetate hydrate (Yb(OAc)₃·xH₂O, 99.9%, Alfa Aesar) was refluxed in glacial acetic acid for 1 h and stored in a desiccator prior to use.
- **2.2.** Nanocrystal Synthesis. Doped CsPb X_3 (X = Cl and Br) NCs were synthesized as detailed previously.³ In a typical synthesis, Yb(OAc)₃ (0-12 mg), Gd(OAc)₃ (0-12 mg), Pb(OAc)₂·3H₂O (76 mg), ODE (5.0 mL), OA (1.0 mL), OAm (0.25 mL), and 1 M CsOAc in EtOH (0.28 mL) were combined in an oven-dried roundbottom flask and degassed on a Schlenk line for 1 h at 110 °C. The flask was then flushed with N2 and heated to 240 °C, whereupon a room-temperature TMS-X solution prepared in a nitrogen-filled glovebox (0.2 mL TMS-X and 0.5 mL anhydrous ODE) was injected into the flask. Following the injection, the reaction vessel was immediately cooled using a room-temperature water bath. The reaction vessel with the resulting NC solution was transferred to a nitrogen-filled glovebox, where the solution was centrifuged at 6000 rpm for 10 min. The supernatant was discarded, leaving a white Gd³⁺doped, Yb3+-doped, or Gd3+/Yb3+-codoped CsPbCl3 or yellow Yb3+doped CsPbBr3 NC pellet. The NC pellet was resuspended in nhexane and flocculated out of the solution with EtOAc. The suspension was then centrifuged again for 10 min, and the supernatant was discarded. The resulting pellet was resuspended in n-hexane and centrifuged for another 15 min. This solution containing the NCs was stored in anhydrous hexane in a nitrogen glovebox. Table S1 summarizes the array of NCs investigated in this study (including those made by anion exchange; see below).
- **2.3.** Anion Exchange Using TMS-Br. Yb³⁺-doped CsPb- $(Cl_{1-x}Br_x)_3$ NCs were prepared by anion exchange using Yb³⁺:CsPbCl₃ NCs according to protocols described previously. 5,28,29

- Briefly, the Yb³⁺:CsPbCl₃ NC solution stored in a nitrogen-filled glovebox was titrated with 1 M TMS-Br until the desired band gap was achieved, as determined by photoluminescence (PL) spectroscopy at room temperature. The residual TMS-Br and solvent were removed by vacuum evaporation, and the resulting NCs were then resuspended in anhydrous hexane and stored in a nitrogen glovebox.
- **2.4. Anion Exchange Using OAm-HCI.** Yb³⁺-doped CsPbCl₃ NCs were prepared by anion exchange using Yb³⁺-doped CsPbBr₃ NCs according to protocols, as detailed previously.⁵ In detail, oleylammonium chloride (OAm-HCl) was synthesized by reacting oleylamine with HCl in a 1:1 (v/v) solution of hexane and toluene. Yb³⁺-doped CsPbBr₃ NCs were titrated with an OAm-HCl solution.
- 2.5. Physical Characterization. The elemental composition of the NC samples was determined using inductively coupled plasmaatomic emission spectroscopy (ICP-AES, PerkinElmer 8300). The doped NC samples were prepared by digesting NC powders in concentrated nitric acid overnight with ultrasonication. Then, the nitric acid mixture was diluted in ultrapure H2O. All dopant concentrations in perovskites were determined as the B-site cation mole fraction (in %). Transmission electron microscopy (TEM) images were obtained by using an FEI TECNAI F20 microscope operating at 200 kV. TEM samples were prepared by drop-casting NCs onto ultrathin carbon-coated copper grids (TED Pella, Inc.). Powder X-ray diffraction (PXRD) data were collected using a Bruker D8 DISCOVER with a high-efficiency IµS microfocus X-ray source for Cu K α radiation (50 kV, 1 mA). Samples for XRD measurements were prepared by drop-casting NC suspensions onto silicon substrates.
- **2.6. Spectroscopic Measurements.** Absorption spectra were collected using an Agilent Cary 5000 spectrometer operating in transmission mode. Samples for PL and time-resolved PL (TRPL) measurements were prepared by drop-casting NCs onto quartz disks and cooling them to 5 K in a closed-cycle helium cryostat (Janis, SHI-4H-5). All PL spectra were measured at each temperature using a 375 nm light-emitting diode (LED) for excitation, operating at \sim 0.6 mW/cm² and using a LN₂-cooled silicon charge-coupled device (CCD) camera mounted on a 0.5 m single monochromator. Spectral bandwidths were kept at 0.38 nm (\sim 3.87 cm $^{-1}$) and 0.03 nm (\sim 0.3 cm $^{-1}$) for room-temperature and high-resolution PL data, respectively. The samples were excited directly with a 375 nm LED and attenuated with neutral density filters as needed, and the signal was detected by using the CCD camera.
- **2.7. Modeling.** All first-principles calculations were performed with the Vienna ab initio simulation package (VASP). 30,31 Plane-wave, Kohn–Sham density functional theory (DFT) calculations employed the all-electron projector augmented wave method in the generalized gradient approximation with the semilocal PBEsol functional. $^{32-34}$ In the pseudopotentials, 9 electrons of Cs ($5s^2$ $5p^6$ $6s^1$), 4 electrons of Pb ($6s^2$ $6p^2$), and 7 electrons of Cl ($3s^2$ $3p^5$) were treated as valence electrons, while 13 f-state electrons in the [Xe] $4f^4$ $6s^2$ valence configuration of Yb were treated as frozen core states. A blocked Davidson iteration was used to optimize the electronic degrees of freedom. A plane-wave basis cutoff was set to 400 eV, and a Gammacentered k-point mesh was used for Brillouin zone integration. 35

A combination of a surrogate energy model based on cluster expansions³⁶ and Markov chain Monte Carlo (MCMC) was employed to predict the expected $Yb_{Pb}-X$ coordination environment as a function of halide composition. To simplify the combinatorics in generating a dataset for fitting the energy model, we assumed an ideal cubic perovskite structure for enumerating configurations of Cl-Br and $Yb_{Pb}-V_{Pb}$ on their respective sublattices. We assumed, furthermore, that both Yb_{Pb} and V_{Pb} exist in their nominal charge states and constrained our simulation cells to be charge-neutral by only allowing for multiples of the fully compensated complex 2Ybpb + V_{Pb}, whether dissociated or not. We employed the SHRY software library³⁷ to enumerate symmetrically distinct Yb_{Pb}-V_{Pb} configurations under this charge-balance constraint. Given the minimum supercell sizes required to fit the longest conformation of these Pb-sublattice defect configurations, we subsequently used random uniform enumeration of the Cl-Br-site decorations. Initial configurations for

subsequent DFT relaxation were generated up to $2 \times 2 \times 3$ supercells, and to improve convergence times, lattice constants for a given halide composition were initialized according to Vegard's law.

After obtaining a sufficiently large dataset of DFT calculations, we fit a cluster expansion model to an intrinsic mixing energy, where the absolute DFT energy for a given configuration was referenced to a linear combination of compositional endpoints (CsPbX3, PbX2, and YbX3) weighted by the halide fraction and the fractional Pb-sublattice concentrations of YbPb and VPb. To reduce the number of cluster expansion terms and improve the convergence of model fitting, we further subtracted a longer-range electrostatic contribution approximated by Ewald summation (accounting for periodic interactions between YbPb and VPb from the total energy. Cluster expansion calculations were facilitated by the ICET software library and model fitting utilized automatic relevance determination regression and 10-fold cross-validation as implemented in the scikit-learn library. 39

Thermodynamic averages of local Yb_{Pb} —X coordination environments were obtained by sampling equilibrium lattice-site occupancy configurations in the canonical ensemble using Metropolis MCMC. To obtain sufficient statistics, each MCMC simulation for a fixed composition was run for at least 1000 sweeps through the lattice, and finite size effects were mitigated by sampling sufficiently large simulation cells. Statistics were gathered for fixed compositions by doing multistart runs initialized at room temperature.

3. RESULTS AND DISCUSSION

3.1. Halide Alloying. 3.1.1. General Characterization. Yb³⁺-doped CsPbCl₃ (x = 0.00) NCs were prepared as

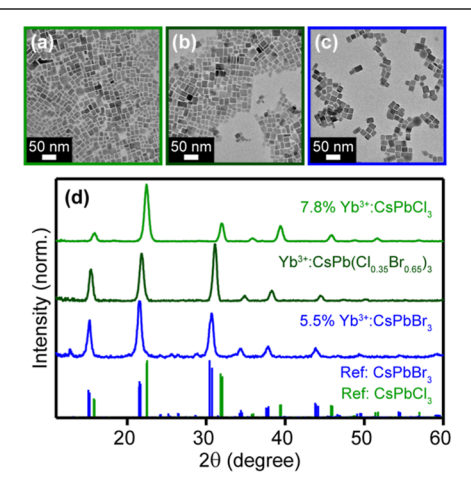


Figure 1. Representative TEM images and PXRD data for Yb^{3+} :CsPb($Cl_{1-x}Br_x)_3$ NCs. (a) 7.8% Yb^{3+} :CsPbCl $_3$ NCs, (b) Yb^{3+} :CsPb($Cl_{0.35}Br_{0.65})_3$ NCs made by anion exchange from the NCs of (a), and (c) 5.5% Yb^{3+} :CsPbBr $_3$ NCs made by direct synthesis. (d) PXRD data collected (light green, top) for the same Yb^{3+} :CsPbCl $_3$, (dark green, middle) Yb^{3+} :CsPb($Cl_{0.0.35}Br_{0.65})_3$, and (blue, bottom) Yb^{3+} :CsPbBr $_3$ NCs made by direct synthesis. Reference indices for the cubic high-temperature forms of CsPbCl $_3$ (green) and CsPbBr $_3$ (blue) are shown at the bottom. Although CsPbCl $_3$ and CsPbBr $_3$ adopt the orthorhombic structure (space group Pnma) at room temperature, the resulting peak splittings are not detectable on the scale plotted here.

described previously.³ Yb³⁺-doped CsPb(Cl_{1-x}Br_x)₃ NCs were prepared by anion exchange from those Yb³⁺:CsPbCl₃ NCs using TMS-Br, following the methods described previously.^{5,28,29,40} Yb³⁺-doped CsPbBr₃ NCs (x = 1.00) were synthesized directly by hot injection of TMS-Br. Figure 1 summarizes representative structural data for a series of Yb³⁺-doped CsPb(Cl_{1-x}Br_x)₃ NCs ranging from $0.00 \le x \le 1.00$. The TEM image of 7.8% Yb³⁺:CsPbCl₃ NCs in Figure 1a

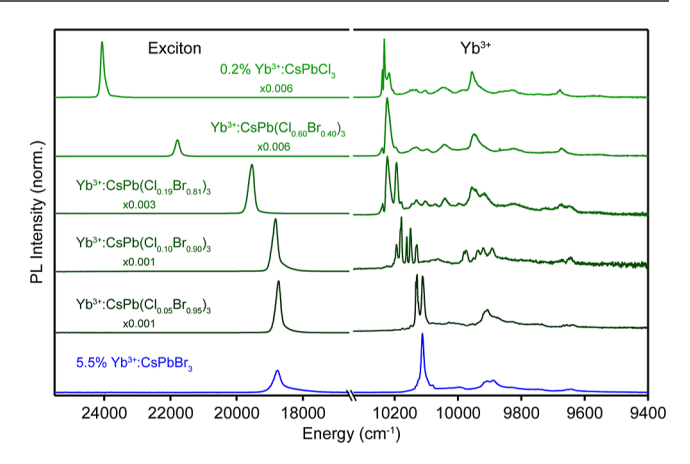


Figure 2. 5 K PL spectra of a series of Yb³⁺:CsPb(Cl_{1-x}Br_x)₃ NCs with different Br⁻ mole fractions: (light green) 0.2% Yb³⁺:CsPbCl₃ NCs, (dark green) various 0.2% Yb³⁺:CsPb(Cl_{1-x}Br_x)₃ NC samples prepared from the same Yb³⁺:CsPbCl₃ NCs by partial anion exchange, and (blue) 5.5% Yb³⁺:CsPbBr₃ NCs prepared by direct synthesis. $\lambda_{\rm ex}$ = 375 nm (26,700 cm⁻¹). From top to bottom, the exciton region has been multiplied by 0.006, 0.006, 0.003, 0.001, 0.001, and 1.0 to display it on the same scale as the Yb³⁺ PL.

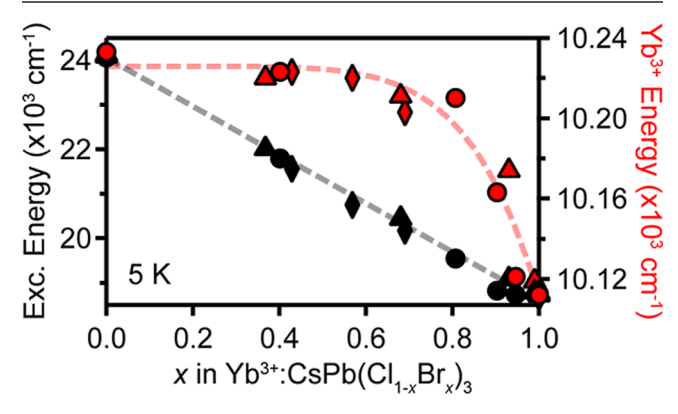


Figure 3. Dependence of the excitonic energies (black) and average Yb³⁺ first electronic origin energies (red) on x, taken from the 5 K PL spectra of various Yb³⁺:CsPb(Cl_{1-x}Br_x)₃ NCs: (circles) the Yb³⁺:CsPb(Cl_{1-x}Br_x)₃ NCs of Figure 2, (triangles) the 7.8% Yb³⁺:CsPb(Cl_{1-x}Br_x)₃ NCs of Figure S5, and (diamonds) the 3.5% Yb³⁺:CsPb(Cl_{1-x}Br_x)₃ NCs of Figure S4. Values of x for each sample were determined from PXRD data using Vegard's law. Dashed lines are guides for the eye.

shows an average edge length of 13.9 ± 2.5 nm, consistent with previous findings. 3,5,23,41 The average edge length of the 7.8% Yb $^{3+}$:CsPb(Cl $_{0.35}$ Br $_{0.65}$) $_3$ NCs in Figure 1b is slightly larger (14.9 \pm 2.7 nm), which reflects the increased ionic radius of Br $^{-.5}$ Figure 1c shows a TEM image of 5.5% Yb $^{3+}$:CsPbBr $_3$ NCs, whose average edge length is 17.4 ± 2.3 nm. Figure 1d shows PXRD patterns collected from the same 7.8% Yb $^{3+}$:CsPbCl $_3$ and 7.8% Yb $^{3+}$:CsPb(Cl $_{0.35}$ Br $_{0.65}$) $_3$ NCs, as well as from 5.5% Yb $^{3+}$:CsPbBr $_3$ NCs. The data show intensities consistent with the reference perovskite structure without any detectable impurities. As reported previously, doping trivalent rare-earth ions (RE $^{3+}$) into CsPbX $_3$ NCs does not cause observable shifts of the XRD reflections or any obvious changes to the NC morphology. $^{3-5,19,23,24,41}$

3.1.2. Effects of Anion Exchange on Yb^{3+} Speciation and Spectroscopy. Figure 2 shows steady-state PL spectra of a series of Yb^{3+} :CsPb(Cl_{1-x}Br_x)₃ (0.00 $\leq x \leq$ 1.00) NCs, all measured at 5 K. Due to the very low dopant concentrations

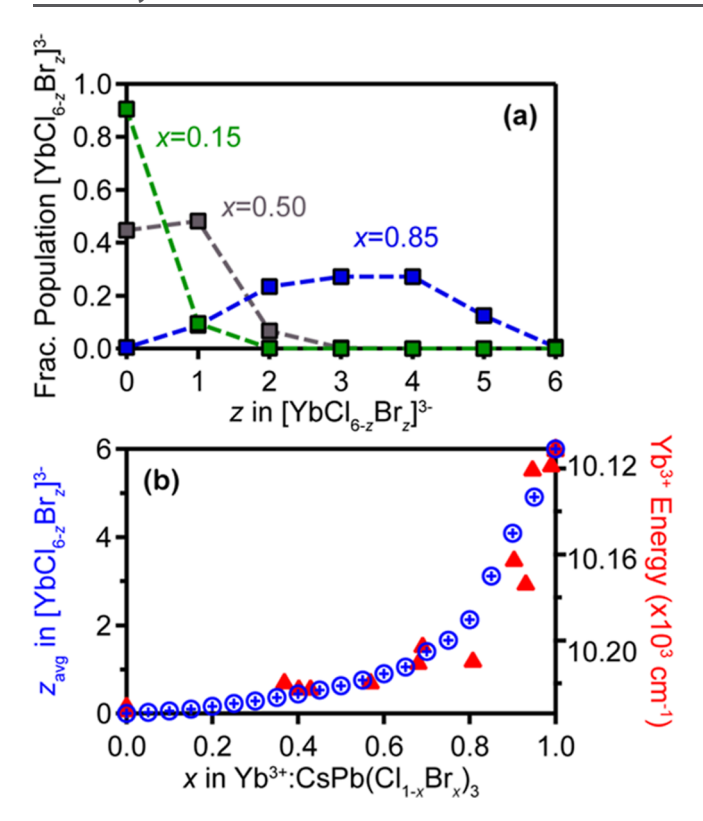


Figure 4. (a) Room-temperature Monte Carlo simulation of the fractional population of $[YbCl_{6-z}Br_z]^{3-}$ ($0 \le z \le 6$) species in 5.0% Yb^{3+} :CsPb($Cl_{1-x}Br_x$) $_3$ at x=0.15 (green), 0.50 (gray), and 0.85 (blue), plotted as a function of z. (b) Average value of z (z_{avg}) in 5.0% Yb^{3+} :CsPb($Cl_{1-x}Br_x$) $_3$, plotted against x. The red data points show the average Yb^{3+} first electronic origin energies from Figure 3 for comparison.

used in all but the CsPbBr3 NCs, the excitonic PL intensities are large and have therefore been scaled for clarity. Looking first at the endpoints (x = 0.00 and 1.00), the Yb³⁺ PL spectra in CsPbCl₃ and CsPbBr₃ lattices show their most intense features at 10,233 and 10,113 cm $^{-1}$, respectively, attributed to the first electronic origin ($\Gamma_8 \to \Gamma_6$, split by low symmetry) of the characteristic set of $^2F_{5/2} \to ^2F_{7/2}$ transitions. These intense peaks are followed by sets of broader and less intense peaks in each sample, which can be attributed to a combination of electronic origins and vibronic sidebands. These spectra and their dependence on the halide are generally similar to those seen in other chloride and bromide lattices, 43 and are consistent with pseudo-octahedral $[YbX_6]^{3-}$, i.e., a slight deviation from octahedral symmetry. These endpoint spectra thus define the coordination limits of [YbCl₆]³⁻ and [YbBr₆]³⁻. As described previously²³ for Yb³⁺:CsPbCl₃ and expanded upon below, multiple Yb³⁺ species are observable in each limiting composition, attributed to electrostatic variations in the second (or beyond) coordination spheres.

With increasing x, the excitonic PL gradually and uniformly shifts to lower energy, reflecting the well-known decrease in the energy gap_g of the perovskite. Starting from CsPbCl₃, small amounts of Br⁻ appear to have little effect on the Yb³⁺ PL energy, although the spectrum broadens somewhat. The Yb³⁺ PL energy begins to shift substantially only at relatively large values of x. In this regime, the redshift is accompanied by the appearance of multiple new sharp peaks in the first electronic origin region (\sim 10,240-10,100 cm⁻¹). These changes are also

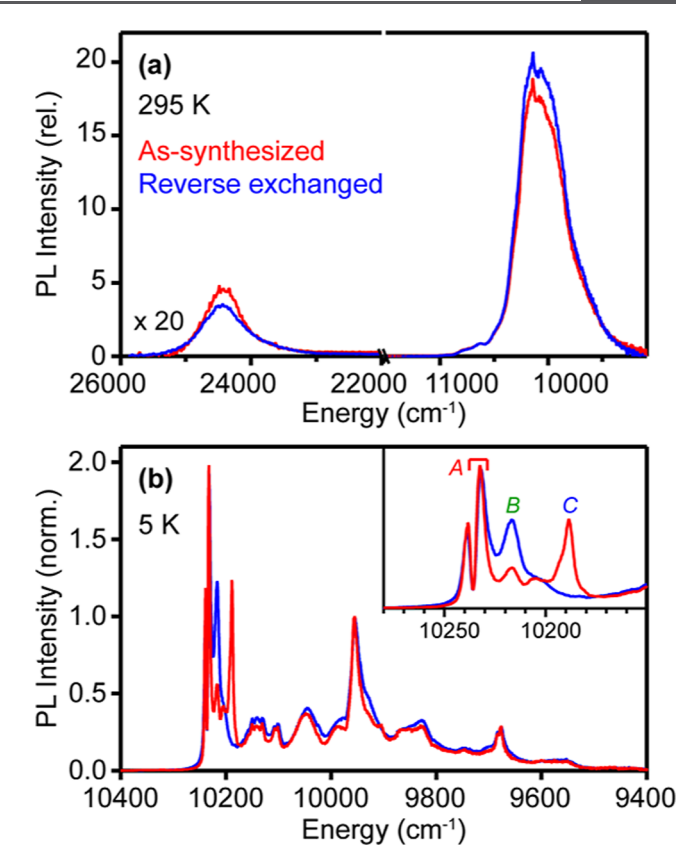


Figure 5. (a) Room-temperature PL spectra of 7.8% Yb³⁺:CsPbCl₃ NCs before (red) and after (blue) a full Cl \rightarrow Br \rightarrow Cl anion exchange/reverse-anion-exchange cycle ($x=0.00 \rightarrow \sim 1.00 \rightarrow \sim 0.00$). Sample photoexcitation rates are equal, such that intensity changes correspond to changes in the relative PLQY. (b) 5 K PL spectra of the same NCs, normalized to the peak maximum at ~ 9960 cm⁻¹. Inset: expansion around the Yb³⁺ first electronic origin shows peaks from multiple Yb³⁺ species. CW excitation at $\lambda_{\rm ex}=375$ nm (26,700 cm⁻¹).

reflected in the energies and widths of the less intense peaks to lower energy, but those are not as well resolved. The observation of multiple resolved peaks around the first electronic origin suggests multiple Yb³+ species with mixed Cl/Br coordination, i.e., distributions of [Yb(Cl_{6-z}Br_z)]³- (0 ≤ $z \leq 6$) populations at intermediate values of x, as expected.

The observations in Figure 2 are summarized in Figure 3, which plots the peak energies of the excitonic PL and the intensity-weighted average energies of the first $Yb^{3+2}F_{7/2} \rightarrow {}^2F_{5/2}$ electronic origin (~10,240–10,100 cm⁻¹) vs x. The excitonic PL energy decreases linearly with increasing x, as expected. 5,8,47 In contrast, the Yb³⁺ PL energy shows little change until $x > \sim 0.5$, at which point it rapidly decreases to approach the energy of Yb³⁺:CsPbBr₃. The divergence between these two curves suggests that the local halide coordination around Yb3+ is not the same as that of the rest of the lattice; i.e., the Yb³⁺ coordination is nonstatistical. To test whether this observation is reproducible, analogous 5 K PL data were collected for two more anion-exchange series (with [Yb³⁺] = 7.8 and 3.5%) as well as for a sample of 7.8% Yb³⁺:CsPbBr₃ NCs prepared by direct synthesis. The curve is highly reproducible, showing that this trend is independent of the specific sample or its specific Yb³⁺ concentration.

Anions are highly mobile in CsPbX₃ NCs, as evidenced by their facile postsynthetic anion exchange.⁸ We therefore

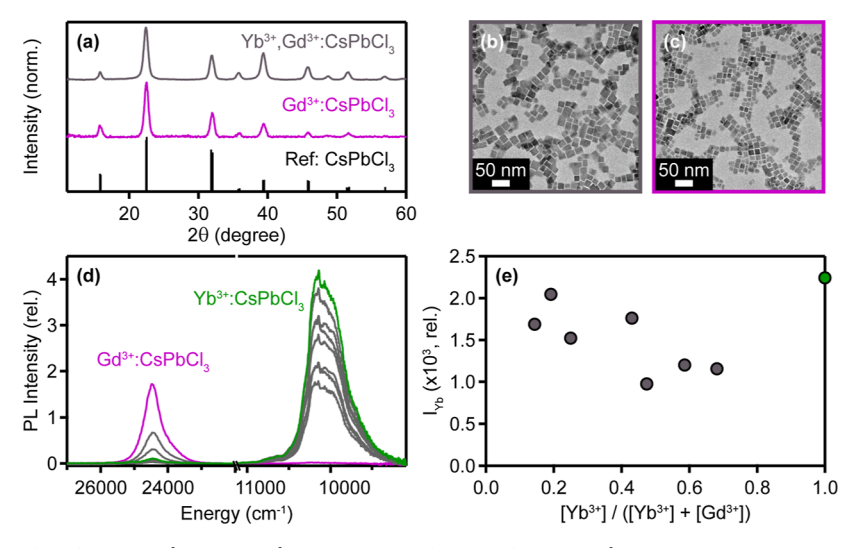


Figure 6. (a) PXRD data for (gray) 5.4% Yb³⁺/2.5% Gd³⁺:CsPbCl₃ and (magenta) 6.8% Gd³⁺:CsPbCl₃ NCs. Reference indices (black) are shown for the cubic high-temperature form of CsPbCl₃. Representative TEM images of the same (b) Yb³⁺/Gd³⁺:CsPbCl₃ and (c) Gd³⁺:CsPbCl₃ NCs. (d) Room-temperature PL spectra of (green) 6.6% Yb³⁺:CsPbCl₃ NCs, (gray) various 0.9–6.9% Yb³⁺/2.5–7.7% Gd³⁺:CsPbCl₃ NCs, and (magenta) 6.8% Gd³⁺:CsPbCl₃ NCs. (e) Integrated Yb³⁺ (²F_{5/2} → ²F_{7/2}) PL intensities for the Yb³⁺:CsPbCl₃ (green) and Yb³⁺/Gd³⁺:CsPbCl₃ (gray) NCs from panel (d), plotted vs [Yb³⁺]/([Yb³⁺] + [Gd³⁺]). All measurements used CW excitation at $λ_{ex}$ = 375 nm (26,700 cm⁻¹), using a constant per-NC excitation rate of 100 s⁻¹.

hypothesize that the nonstatistical anion distributions within these Yb³⁺:CsPb(Cl_{1-x}Br_x)₃ NCs reflect lattice thermodynamics, not kinetics. To understand this observation, it is helpful to compare the relevant bond dissociation energies: 385 kJ/mol for Yb–Cl (YbCl₃) and 322 kJ/mol for Yb–Br (YbBr₃), compared to 304 kJ/mol for Pb–Cl (PbCl₂) and 260 kJ/mol for Pb–Br (PbBr₂).⁴⁸ From these numbers, a driving force for retaining Yb–Cl bonds in Yb³⁺:CsPb(Cl_{1-x}Br_x)₃ of ~20 kJ/mol Cl⁻ anion may be anticipated. We hypothesize that Yb³⁺ itself may migrate and cluster together to minimize the total energy, including from lattice strain. A similar scenario was observed⁴⁰ to cause spontaneous aggregation of [MnCl₆]⁴⁻ units with increasing *x* in Mn²⁺-doped CsPb(Cl_{1-x}Br_x)₃ NCs.

To explore the thermodynamics of anion alloying in these doped NCs further, we employed canonical Monte Carlo simulations. Calculations were performed on model systems of 5% Yb³⁺:CsPb(Cl_{1-x}Br_x)₃ at room temperature (see the Experimental Section). Figure 4a plots the equilibrium populations of all possible [YbCl_{6-z}Br_z]³⁻ species calculated for x = 0.15, 0.50, and 0.85 (see Figure S7 for more compositions). At x = 0.15, nearly all Yb³⁺ ions have exclusive Cl^- coordination (z = 0). Increasing x shifts the species distribution to a higher z, but at x = 0.50, the distribution remains highly skewed toward a small z. Not until x = 0.85 is the distribution centered roughly at z = 3, and even when x =0.95, ~20% of the halides surrounding Yb3+ are still Cl- ions (Figure S7). These results show that the halide distribution in the first coordination sphere of Yb3+ is highly nonstatistical, with Cl⁻ strongly favored. Figure 4b replots the results from Figure 4a to show the average number of Br⁻ ions (z_{avg}) bound to Yb³⁺ as a function of x. Overlaid with these data are the Yb³⁺ PL energies from Figure 3, scaled to highlight the similarity of the two curves. For both the experimental and computed results, the data show that most anion substitution at Yb3+ occurs only at large x, i.e., Yb^{3+} ions preferentially bind Cl^{-} in Yb^{3+} : $CsPb(Cl_{1-x}Br_x)_3$.

To probe for structural reorganization during anion exchange, we compared the 5 K Yb³⁺ PL of Yb³⁺:CsPbCl₃

measured before anion exchange with that measured after complete anion exchange followed by complete reverse anion exchange: 7.8% Yb3+:CsPbCl3 NCs were first converted to Yb³⁺:CsPbBr₃ NCs, and then Cl⁻ anions were reintroduced to convert them back to Yb³⁺:CsPbCl₃ NCs. Figure 5a plots the room-temperature PL spectra for these two samples collected at the same photoexcitation rate, and Figure 5b plots the 5 K PL spectra of the same samples normalized to the peak maximum at \sim 9960 cm⁻¹. The room-temperature spectra are very similar, but the 5 K spectra show marked differences in the intensities of the minority species emitting at energies just below the first intense electronic origin (~10,190-10,230 cm⁻¹). Three main features in this region can be identified and attributed to the first electronic origins of three different species: A, B, and C. The as-prepared Yb3+:CsPbCl3 NCs show a prominent feature from species C that disappears following the anion-exchange cycle. These extra PL features result from having different local electrostatic environments around some subset of Yb³⁺ dopants, i.e., beyond the first coordination sphere. The fact that these electrostatic changes occur during the anion exchange/reverse-anion-exchange cycle indicates some degree of additional lattice restructuring during anion exchange beyond simply swapping anions; these spectroscopic changes would not be observed if anion exchange only replaced all of the anions and left the rest of the lattice unchanged. Interestingly, this substantial change in Yb3+ speciation has little effect on the relative room-temperature Yb³⁺ PLQY, which actually increases by \sim 10% following the anion exchange/reverse-anion-exchange cycle (Figure 5a), similar to our previous observations.³

3.2. B-Site Cation Alloying. 3.2.1. General Characterization. Previous studies have reported improved quantum cutting in Yb³⁺:CsPb(Cl_{1-x}Br_x)₃ samples codoped with additional RE³⁺ ions, attributed to the reduction of non-radiative losses. 2,14,49 To explore the effects of RE³⁺ codoping on Yb³⁺ speciation and quantum cutting, we investigated the properties of Yb³⁺/Gd³⁺-codoped CsPbCl₃ NCs. Previous work showed that Gd³⁺ and other spectroscopically innocent

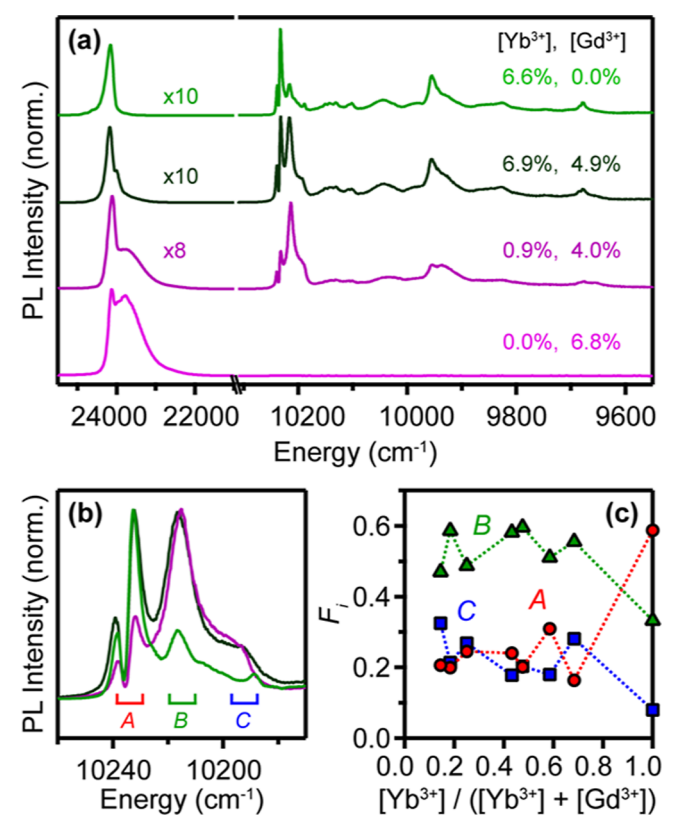


Figure 7. (a) 5 K PL spectra of the NCs in Figure 6: (light green) 6.6% Yb³⁺:CsPbCl₃, (dark green) 6.9% Yb³⁺/4.9% Gd³⁺:CsPbCl₃, (purple) 0.9% Yb³⁺/4.0% Gd³⁺:CsPbCl₃, and (magenta) 6.8% Gd³⁺:CsPbCl₃. $\lambda_{\rm ex}=375$ nm (26,700 cm⁻¹). From top to bottom, the exciton region has been multiplied by 10, 10, 8, and 1 to display it on the same scale as the Yb³⁺ PL. (b) Expanded view of the Yb³⁺ first electronic origin region from (a), showing peaks associated with three Yb³⁺ species: *A*, *B*, and *C*. (c) The fractional integrated intensities (F_i) of species *A* (red), *B* (green), and *C* (blue) observed in the spectra of various Yb³⁺/Gd³⁺:CsPbCl₃ NCs, taken from the 5 K PL spectra of panel (a) and Figure S8, plotted vs [Yb³⁺]/([Yb³⁺] + [Gd³⁺]).

RE³⁺ dopants universally generate a similar near-band-edge defect state, 3,47 attributed to charge-compensating V_{Pb} defects. Codoping with Gd^{3+} is thus expected to introduce additional V_{Pb} and, in the case of low Yb^{3+} doping and high Gd^{3+} doping, the occurrence of correlated $\left[Yb_{Pb}\!-\!V_{Pb}\!-\!Yb_{Pb}\right]^0$ pairs should be largely suppressed. B-site alloying thus provides the opportunity to probe the importance of the colocalization of two Yb^{3+} ions on PL sensitization.

Yb³⁺/Gd³⁺ codoped CsPbCl₃ NCs were prepared by simply adding Gd(OAc)₃ in addition to the Yb(OAc)₃ precursor at the desired ratio (see Experimental Section). Figure 6a shows PXRD data collected for 5.4% Yb³⁺/2.5% Gd³⁺:CsPbCl₃ and 6.8% Gd³⁺:CsPbCl₃ NCs. These data resemble those of other RE³⁺-doped CsPbCl₃ NCs. 3,23,47,50 As with Yb³⁺ doping, Gd³⁺ doping does not cause significant shifts in the XRD peak positions relative to CsPbCl₃. TEM images of the Yb³⁺/Gd³⁺:CsPbCl₃ and Gd³⁺:CsPbCl₃ NCs from Figure 6a show average edge lengths of 16.9 \pm 3.8 nm (Figure 6b) and 12.8 \pm 2.6 nm (Figure 6c), which are typical of this synthesis.

Figure 6d plots room-temperature PL spectra of the 6.8% Gd³⁺:CsPbCl₃ NCs from Figure 6a, as well as of several other Yb³⁺/Gd³⁺:CsPbCl₃ NCs with various RE³⁺ concentration levels (0.9–6.9% Yb³⁺/2.5–7.7% Gd³⁺). The Gd³⁺:CsPbCl₃ NCs show near-band-edge PL and no NIR luminescence, while

the Yb³+-doped CsPbCl₃ NCs show strong ${}^2F_{5/2} \rightarrow {}^2F_{7/2}$ PL in the NIR and weak excitonic PL. When compared to Yb³+:CsPbCl₃ NCs with similar Yb³+ concentrations, codoped samples show more excitonic PL and comparable Yb³+ PL intensities. Figure 6e summarizes the results of Figure 6d by plotting the integrated Yb³+ PL intensity vs [Yb³+]/([Yb³+] + [Gd³+]). Despite the large differences in B-site composition, Yb³+ sensitization remains constant within a factor of 2 across this series. Most notably, samples with low and high [Yb³+] show similar NIR PL intensities, representing a departure from the usual trend of increasing NIR PL with increasing [Yb³+].³

3.2.2. Effects of B-Site Cation Alloying on Yb^{3+} Speciation and Spectroscopy. To explore the above conclusions in more detail, high-resolution PL measurements were used to probe whether Gd^{3+} codoping indeed causes any noticeable change in Yb^{3+} speciation. Figure 7a shows 5 K steady-state PL spectra measured for the 6.6% Yb^{3+} :CsPbCl₃ and 6.8% Gd^{3+} :CsPbCl₃ NCs from Figure 6, as well as for two Yb^{3+}/Gd^{3+} :CsPbCl₃ NC samples with similar total B-site dopant concentrations. The Gd^{3+} :CsPbCl₃ NCs show excitonic PL accompanied by the characteristic shallow-defect band \sim 400 cm⁻¹ lower in energy, as detailed previously. The intensities of these features decrease as $[Yb^{3+}]/([Yb^{3+}] + [Gd^{3+}])$ increases until ultimately the shallow-defect emission is not observed in Yb^{3+} :CsPbCl₃ NCs. These observations are consistent with the depletion of the shallow-trap state via energy transfer to Yb^{3+} .

Although the Yb³⁺ PL spectra of the samples in Figure 7a are all generally similar, new features are resolved near the first electronic origin (~10,240-10,180 cm⁻¹) upon Gd³⁺ codoping. These features are precisely the same as those observed in the Yb3+:CsPbCl3 NCs of Figure 5 but with different relative intensities, and they are similarly attributable to Yb3+ species with different local electrostatic environments beyond the [YbCl₆]³⁻ first coordination sphere. Figure 7c plots the 5 K fractional integrated intensities (F_i) of these three peaks against $[Yb^{3+}]/([Yb^{3+}] + [Gd^{3+}])$ for the samples from Figure 7a as well as for additional samples from Figure S8. Upon introduction of Gd^{3+} , F_A drops rapidly while F_B and F_C increase. These three species also differ in their PL temperature dependence (Figure S11). Crucially, codoping with Gd³⁺ disrupts the formation of proximal [Yb_{Pb}-V_{Pb}-Yb_{Pb}]⁰ pairs, and for the extreme case of 0.9% Yb3+/4.0% Gd3+:CsPbCl3 NCs of Figure 7, virtually none of these pairs are expected, replaced instead by $[Yb_{Pb}-V_{Pb}-Gd_{Pb}]^0$ pairs (in addition to various partially $([Yb_{Pb}-V_{Pb}]^1)$ and completely $([Yb_{Pb}]^1)$ dissociated configurations²⁶). The increase in peaks B and C in this sample relative to the 6.6% Yb3+:CsPbCl3 NCs of Figure 7 indicates that this PL must be associated with isolated Yb3+ ions in some way rather than with Yb3+...Yb3+ pairs. Interestingly, species A dominates the quantum-cutting PL spectrum of Yb³⁺:CsPbCl₃, but these results combined with those in Figure 6e show that species B and C can also yield similarly efficient Yb³⁺ PL sensitization. Although the precise microscopic identities of species A, B, and C are unclear, these results demonstrate that quantum cutting in Yb3+:CsPbCl3 is tolerant of variations in the microscopic configuration of Yb³⁺ ions. In particular, it is not necessary for participating Yb³⁺ ions to be immediate neighbors to accept energy via quantum cutting. This conclusion is consistent with the small binding energy of the shallow-trap state believed to mediate quantum cutting, which endows that state with a relatively large effective radius²⁶ that allows it to couple with two nonproximal Yb³⁺ ions simultaneously.

4. CONCLUSIONS

The relationship between Yb3+ sensitization and speciation in doped CsPb(Cl_{1-x}Br_x)₃ perovskite NCs has been investigated by combining systematic changes in lattice composition with low-temperature high-resolution PL spectroscopy to track the evolution of Yb³⁺ speciation with these changes. Introduction of Br⁻ changes the local halide coordination around Yb³⁺ ions but is distinctly nonstatistical, indicating a thermodynamic preference for retention of Yb-Cl bonds even in the presence of large amounts of lattice Br⁻. Addition of Gd³⁺ codopants to Yb^{3+} :CsPbCl₃ disrupts the formation of proximal [Yb_{Pb} - V_{Pb} - $Yb_{Pb}]^0$ pairs and increases the ratio of V_{Pb} to Yb^{3+} ions. Codoping has little effect on the efficiency of Yb3+ sensitization but alters the primary Yb3+ speciation, highlighting the tolerance of quantum cutting to variations in the specific identities of participating Yb3+ ions and, in particular, to the spatial separation between them. These results enhance our fundamental understanding of structure-function relationships in Yb³⁺:CsPb(Cl_{1-x}Br_x)₃ quantum cutters, with ramifications for their optimization and development for future optoelectronic applications.

ASSOCIATED CONTENT

Supporting Information

The Supporting Information is available free of charge at https://pubs.acs.org/doi/10.1021/acs.chemmater.3c01475.

Additional TEM, XRD data, room-temperature absorption, variable-temperature PL spectra, and Monte Carlo data (PDF)

AUTHOR INFORMATION

Corresponding Author

Daniel R. Gamelin — Department of Chemistry, University of Washington, Seattle, Washington 98195, United States; orcid.org/0000-0003-2888-9916; Email: gamelin@uw.edu

Authors

Joo Yeon D. Roh — Department of Chemistry, University of Washington, Seattle, Washington 98195, United States; orcid.org/0000-0001-9801-3069

David E. Sommer — Department of Physics, University of Washington, Seattle, Washington 98195, United States

Tyler J. Milstein — Department of Chemistry, University of Washington, Seattle, Washington 98195, United States;

orcid.org/0000-0002-1517-2222

Scott T. Dunham – Department of Electrical & Computer Engineering, University of Washington, Seattle, Washington 98195, United States

Complete contact information is available at: https://pubs.acs.org/10.1021/acs.chemmater.3c01475

Notes

The authors declare no competing financial interest.

ACKNOWLEDGMENTS

This work was primarily supported by the U.S. National Science Foundation through the University of Washington Molecular Engineering Materials Center, a Materials Research Science and Engineering Center (DMR-1719797 and DMR-2308979). The early stages of this work were performed with the support of NSF DMR-1807394. Part of this work was

conducted at the University of Washington Molecular Analysis Facility, a National Nanotechnology Coordinated Infrastructure site supported in part by funds from the National Science Foundation (awards NNCI-2025489 and NNCI-1542101), the Molecular Engineering & Sciences Institute, and the Clean Energy Institute. The authors thank K. T. Kluherz for acquiring TEM images and J. J. Araujo for acquiring PXRD data.

REFERENCES

- (1) Pan, G.; Bai, X.; Yang, D.; Chen, X.; Jing, P.; Qu, S.; Zhang, L.; Zhou, D.; Zhu, J.; Xu, W.; et al. Doping Lanthanide into Perovskite Nanocrystals: Highly Improved and Expanded Optical Properties. *Nano Lett.* **2017**, *17*, 8005–8011.
- (2) Zhou, D.; Liu, D.; Pan, G.; Chen, X.; Li, D.; Xu, W.; Bai, X.; Song, H. Cerium and Ytterbium Codoped Halide Perovskite Quantum Dots: A Novel and Efficient Downconverter for Improving the Performance of Silicon Solar Cells. *Adv. Mater.* **2017**, *29*, 1704149.
- (3) Milstein, T. J.; Kroupa, D. M.; Gamelin, D. R. Picosecond Quantum Cutting Generates Photoluminescence Quantum Yields Over 100% in Ytterbium-Doped CsPbCl₃ Nanocrystals. *Nano Lett.* **2018**, *18*, 3792–3799.
- (4) Kroupa, D. M.; Roh, J. Y.; Milstein, T. J.; Creutz, S. E.; Gamelin, D. R. Quantum-Cutting Ytterbium-Doped CsPb(Cl_{1-x}Br_x)₃ Perovskite Thin Films with Photoluminescence Quantum Yields over 190%. *ACS Energy Lett.* **2018**, *3*, 2390–2395.
- (5) Milstein, T. J.; Kluherz, K. T.; Kroupa, D. M.; Erickson, C. S.; De Yoreo, J. J.; Gamelin, D. R. Anion Exchange and the Quantum-Cutting Energy Threshold in Ytterbium-Doped CsPb(Cl_{1-x}Br_x)₃ Perovskite Nanocrystals. *Nano Lett.* **2019**, *19*, 1931–1937.
- (6) Mir, W. J.; Sheikh, T.; Arfin, H.; Xia, Z.; Nag, A. Lanthanide Doping in Metal Halide Perovskite Nanocrystals: Spectral Shifting, Quantum Cutting and Optoelectronic Applications. *NPG Asia Mater.* **2020**, *12*, 9.
- (7) Zeng, M.; Artizzu, F.; Liu, J.; Singh, S.; Locardi, F.; Mara, D.; Hens, Z.; Van Deun, R. Boosting the Er³⁺ 1.5 μm Luminescence in CsPbCl₃ Perovskite Nanocrystals for Photonic Devices Operating at Telecommunication Wavelengths. ACS Appl. Nano Mater. **2020**, 3, 4699–4707.
- (8) Dey, A.; Ye, J.; De, A.; Debroye, E.; Ha, S. K.; Bladt, E.; Kshirsagar, A. S.; Wang, Z.; Yin, J.; Wang, Y.; et al. State of the Art and Prospects for Halide Perovskite Nanocrystals. *ACS Nano* **2021**, *15*, 10775–10981.
- (9) Vergeer, P.; Vlugt, T. J. H.; Kox, M. H. F.; den Hertog, M. I.; van der Eerden, J. P. J. M.; Meijerink, A. Quantum Cutting by Cooperative Energy Transfer in Yb_xY_{1-x}PO₄:Tb³⁺. *Phys. Rev. B* **2005**, *71*, 014119.
- (10) Lakshminarayana, G.; Yang, H.; Ye, S.; Liu, Y.; Qiu, J. Cooperative Downconversion Luminescence in Pr³⁺/Yb³⁺:SiO₂-Al₂O₃-BaF₂-GdF₃ glasses. *J. Mater. Res.* **2008**, *23*, 3090–3095.
- (11) Lakshminarayana, G.; Yang, H.; Ye, S.; Liu, Y.; Qiu, J. Co-Operative Downconversion Luminescence in Tm³⁺/Yb³⁺: SiO₂-Al₂O₃-LiF-GdF₃ Glasses. *J. Phys. D: Appl. Phys.* **2008**, *41*, 175111.
- (12) Aarts, L.; van der Ende, B. M.; Meijerink, A. Downconversion for Solar Cells in NaYF₄:Er,Yb. *J. Appl. Phys.* **2009**, *106* (2), 023522. (13) Aarts, L.; Jaeqx, S.; van der Ende, B. M.; Meijerink, A. Downconversion for the Er³⁺ Vl³⁺ Couple in KPb Cl.—A Low.

Downconversion for the Er³⁺, Yb³⁺ Couple in KPb₂Cl₅—A Low-Phonon Frequency Host. *J. Lumin.* **2011**, *131*, 608–613.

- (14) Zhou, D.; Sun, R.; Xu, W.; Ding, N.; Li, D.; Chen, X.; Pan, G.; Bai, X.; Song, H. Impact of Host Composition, Codoping, or Tridoping on Quantum-Cutting Emission of Ytterbium in Halide Perovskite Quantum Dots and Solar Cell Applications. *Nano Lett.* **2019**, *19*, 6904–6913.
- (15) Shockley, W.; Queisser, H. J. Detailed Balance Limit of Efficiency of *p-n* Junction Solar Cells. *J. Appl. Phys.* **1961**, 32, 510–519.

- (16) Dexter, D. L. Two Ideas on Energy Transfer Phenomena: Ion-Pair Effects Involving the OH Stretching Mode, and Sensitization of Photovoltaic Cells. *J. Lumin.* **1979**, *18*–19, 779–784.
- (17) Trupke, T.; Green, M. A.; Würfel, P. Improving Solar Cell Efficiencies by Down-Conversion of High-Energy Photons. *J. Appl. Phys.* **2002**, 92, 1668–1674.
- (18) Crane, M. J.; Kroupa, D. M.; Gamelin, D. R. Detailed-Balance Analysis of Yb³⁺:CsPb(Cl_{1-x}Br_x)₃ Quantum-Cutting Layers for High-Efficiency Photovoltaics Under Real-World Conditions. *Energy Environ. Sci.* **2019**, *12*, 2486–2495.
- (19) Cohen, T. A.; Milstein, T. J.; Kroupa, D. M.; MacKenzie, J. D.; Luscombe, C. K.; Gamelin, D. R. Quantum-Cutting Yb³⁺-Doped Perovskite Nanocrystals for Monolithic Bilayer Luminescent Solar Concentrators. *J. Mater. Chem. A* **2019**, *7*, 9279–9288.
- (20) Luo, X.; Ding, T.; Liu, X.; Liu, Y.; Wu, K. Quantum-Cutting Luminescent Solar Concentrators Using Ytterbium-Doped Perovskite Nanocrystals. *Nano Lett.* **2019**, *19*, 338–341.
- (21) Cai, T.; Wang, J.; Li, W.; Hills-Kimball, K.; Yang, H.; Nagaoka, Y.; Yuan, Y.; Zia, R.; Chen, O. Mn²⁺/Yb³⁺ Codoped CsPbCl₃ Perovskite Nanocrystals with Triple-Wavelength Emission for Luminescent Solar Concentrators. *Adv. Sci.* **2020**, *7*, 2001317.
- (22) Ding, N.; Xu, W.; Zhou, D.; Ji, Y.; Wang, Y.; Sun, R.; Bai, X.; Zhou, J.; Song, H. Extremely Efficient Quantum-Cutting Cr³⁺, Ce³⁺, Yb³⁺ Tridoped Perovskite Quantum Dots for Highly Enhancing the Ultraviolet Response of Silicon Photodetectors with External Quantum Efficiency Exceeding 70%. *Nano Energy* **2020**, 78, 105278.
- (23) Roh, J. Y. D.; Smith, M. D.; Crane, M. J.; Biner, D.; Milstein, T. J.; Krämer, K. W.; Gamelin, D. R. Yb³⁺ Speciation and Energy-Transfer Dynamics in Quantum-Cutting Yb³⁺-Doped CsPbCl₃ Perovskite Nanocrystals and Single Crystals. *Phys. Rev. Mater.* **2020**, *4*, 105405.
- (24) Crane, M. J.; Kroupa, D. M.; Roh, J. Y.; Anderson, R. T.; Smith, M. D.; Gamelin, D. R. Single-Source Vapor Deposition of Quantum-Cutting Yb³⁺:CsPb($Cl_{1-x}Br_x$)₃ and Other Complex Metal-Halide Perovskites. ACS Appl. Energy Mater. **2019**, 2, 4560–4565.
- (25) Cleveland, I. J.; Tran, M. N.; Kabra, S.; Sandrakumar, K.; Kannan, H.; Sahu, A.; Aydil, E. S. Physical Vapor Deposition of Yb-Doped CsPbCl₃ Thin Films for Quantum Cutting. *Phys. Rev. Mater.* **2023**, *7*, 065404.
- (26) Sommer, D. E.; Gamelin, D. R.; Dunham, S. T. Defect Formation in Yb-Doped CsPbCl₃ from First Principles with Implications for Quantum Cutting. *Phys. Rev. Mater.* **2022**, *6*, 025404.
- (27) Kluherz, K. T.; Mergelsberg, S. T.; Sommer, D. E.; Roh, J. Y. D.; Saslow, S. A.; Biner, D.; Krämer, K. W.; Dunham, S. T.; De Yoreo, J. J.; Gamelin, D. R. Defect Structure in Quantum-Cutting Yb³⁺-Doped CsPbCl₃ Perovskites Probed by X-Ray Absorption and Atomic Pair Distribution Function Analysis. *Phys. Rev. Mater.* **2022**, *6*, 074601.
- (28) Creutz, S. E.; Crites, E. N.; De Siena, M. C.; Gamelin, D. R. Anion Exchange in Cesium Lead Halide Perovskite Nanocrystals and Thin Films Using Trimethylsilyl Halide Reagents. *Chem. Mater.* **2018**, 30, 4887–4891.
- (29) Creutz, S. E.; Crites, E. N.; De Siena, M. C.; Gamelin, D. R. Colloidal Nanocrystals of Lead-Free Double-Perovskite (Elpasolite) Semiconductors: Synthesis and Anion Exchange To Access New Materials. *Nano Lett.* **2018**, *18*, 1118–1123.
- (30) Kresse, G.; Furthmüller, J. Efficient Iterative Schemes for Ab Initio Total-Energy Calculations Using a Plane-Wave Basis Set. *Phys. Rev. B* **1996**, *54*, 11169–11186.
- (31) Kresse, G.; Furthmüller, J. Efficiency of Ab-Initio Total Energy Calculations for Metals and Semiconductors Using a Plane-Wave Basis Set. *Comput. Mater. Sci.* **1996**, *6*, 15–50.
- (32) Blöchl, P. E. Projector Augmented-Wave Method. *Phys. Rev. B* **1994**, *50*, 17953–17979.
- (33) Kohn, W.; Sham, L. J. Self-Consistent Equations Including Exchange and Correlation Effects. *Phys. Rev.* **1965**, *140*, A1133–A1138.
- (34) Perdew, J. P.; Ruzsinszky, A.; Csonka, G. I.; Vydrov, O. A.; Scuseria, G. E.; Constantin, L. A.; Zhou, X.; Burke, K. Restoring the

- Density-Gradient Expansion for Exchange in Solids and Surfaces. *Phys. Rev. Lett.* **2008**, *100*, 136406.
- (35) Monkhorst, H. J.; Pack, J. D. Special Points for Brillouin-Zone Integrations. *Phys. Rev. B* **1976**, *13*, 5188–5192.
- (36) Sanchez, J. M.; Ducastelle, F.; Gratias, D. Generalized Cluster Description of Multicomponent Systems. *Phys. A* **1984**, *128*, 334–350.
- (37) Prayogo, G. I.; Tirelli, A.; Utimula, K.; Hongo, K.; Maezono, R.; Nakano, K. Shry: Application of Canonical Augmentation to the Atomic Substitution Problem. *J. Chem. Inf. Model.* **2022**, *62*, 2909–2915
- (38) Ångqvist, M.; Muñoz, W. A.; Rahm, J. M.; Fransson, E.; Durniak, C.; Rozyczko, P.; Rod, T. H.; Erhart, P. ICET A Python Library for Constructing and Sampling Alloy Cluster Expansions. *Adv. Theory Simul.* **2019**, 2 (7), 1900015.
- (39) Pedregosa, F.; Varoquaux, G.; Gramfort, A.; Michel, V.; Thirion, B.; Grisel, O.; Blondel, M.; Prettenhofer, P.; Weiss, R.; Dubourg, V.; et al. Scikit-learn: Machine Learning in Python. *J. Mach. Learn. Res.* **2011**, *12*, 2825–2830.
- (40) De Siena, M. C.; Sommer, D. E.; Creutz, S. E.; Dunham, S. T.; Gamelin, D. R. Spinodal Decomposition During Anion Exchange in Colloidal Mn²⁺-Doped CsPbX₃ (X = Cl, Br) Perovskite Nanocrystals. *Chem. Mater.* **2019**, *31*, *7711–7722*.
- (41) Erickson, C. S.; Crane, M. J.; Milstein, T. J.; Gamelin, D. R. Photoluminescence Saturation in Quantum-Cutting Yb³⁺-Doped CsPb(Cl_{1-x}Br_x)₃ Perovskite Nanocrystals: Implications for Solar Downconversion. *J. Phys. Chem. C* **2019**, *123*, 12474–12484.
- (42) Linaburg, M. R.; McClure, E. T.; Majher, J. D.; Woodward, P. M. Cs_{1-x}Rb_xPbCl₃ and Cs_{1-x}Rb_xPbBr₃ Solid Solutions: Understanding Octahedral Tilting in Lead Halide Perovskites. *Chem. Mater.* **2017**, *29*, 3507–3514.
- (43) Tanner, P. A. Electronic Spectra of Yb^{3+} in Elpasolite Lattices. *Mol. Phys.* **1986**, *58*, 317–328.
- (44) Valiente, R.; Wenger, O. S.; Güdel, H. U. Upconversion Luminescence in Yb³⁺ Doped CsMnCl₃: Spectroscopy, Dynamics, and Mechanisms. *J. Chem. Phys.* **2002**, *116*, 5196–5204.
- (45) Hehlen, M. P.; Kuditcher, A.; Rand, S. C.; Tischler, M. A. Electron-Phonon Interactions in CsCdBr₃:Yb³⁺. *J. Chem. Phys.* **1997**, 107, 4886–4892.
- (46) Goldner, P.; Pellé, F.; Meichenin, D.; Auzel, F. Cooperative Luminescence in Ytterbium-Doped CsCdBr₃. *J. Lumin.* **1997**, 71, 137–150.
- (47) Milstein, T. J.; Roh, J. Y. D.; Jacoby, L. M.; Crane, M. J.; Sommer, D. E.; Dunham, S. T.; Gamelin, D. R. Ubiquitous Near-Band-Edge Defect State in Rare-Earth-Doped Lead-Halide Perovskites. *Chem. Mater.* **2022**, *34*, 3759–3769.
- (48) King, R. B.; Crabtree, R. H.; Lukehart, C. M.; Atwood, D. A.; Scott, R. A. Bond Energies. In *Encyclopedia of Inorganic Chemistry*; Wiley, 2006.
- (49) Yang, G.; Zheng, C.; Zhu, Y.; Li, X.; Huang, J.; Xu, X.; Liu, W.; Cui, S.; Pan, G. Efficient Quantum Cutting of Lanthanum and Ytterbium Ions Co-Doped Perovskite Quantum Dots Towards Improving the Ultraviolet Response of Silicon-Based Photodetectors. *J. Alloys Compd.* **2022**, 921, 166097.
- (50) Li, D.; Chen, G. Near-Infrared Photoluminescence from Ytterbium- and Erbium-Codoped CsPbCl₃ Perovskite Quantum Dots with Negative Thermal Quenching. *J. Phys. Chem. Lett.* **2023**, *14*, 2837–2844.